Chemical Science

ROYAL SOCIETY OF CHEMISTRY

EDGE ARTICLE

View Article Online
View Journal | View Issue

Cite this: *Chem. Sci.*, 2024, **15**, 15925

All publication charges for this article have been paid for by the Royal Society of Chemistry

Received 19th April 2024
Accepted 15th August 2024

DOI: 10.1039/d4sc02588a

rsc.li/chemical-science

Ethanol synthesis *via* catalytic CO_2 hydrogenation over multi-elemental KFeCuZn/ZrO_2 catalyst†

Pengfei Du,[a] Abdellah Ait El Fakir,*[a] Shirun Zhao,[a] Nazmul Hasan M. D. Dostagir,[a] HongLi Pan,[a] Kah Wei Ting,[a] Shinya Mine,[b] Yucheng Qian,[a] Ken-ichi Shimizu*[a] and Takashi Toyao*[a]

Technological enablers that use CO_2 as a feedstock to create value-added chemicals, including ethanol, have gained widespread appeal. They offer a potential solution to climate change and promote the development of a circular economy. However, the conversion of CO_2 to ethanol poses significant challenges, not only because CO_2 is a thermodynamically stable and chemically inert molecule but also because of the complexity of the reaction routes and uncontrollability of C–C coupling. In this study, we developed an efficient catalyst, K–Fe–Cu–Zn/ZrO_2 (KFeCuZn/ZrO_2), which enhances the EtOH space time yield (STY_{EtOH}) to 5.4 mmol g_{cat}^{-1} h^{-1}, under optimized conditions (360 °C, 4 MPa, and 12 L g_{cat}^{-1} h^{-1}). Furthermore, we investigated the roles of each constituent element using *in situ*/*operando* spectroscopy such as X-ray absorption spectroscopy (XAS) and diffuse reflectance infrared Fourier transform spectroscopy (DRIFTS). These results demonstrate that all components are necessary for efficient ethanol synthesis.

Introduction

CO_2 hydrogenation into chemicals and fuels is recognized as a pivotal process for achieving a sustainable carbon cycle.[1–4] The CO_2 hydrogenation into C_{2+} alcohols has great industrial significance but is scientifically challenging, primarily because of the intricate reaction mechanisms involved and necessity of forming carbon–carbon (C–C) bonds, resulting in the low selectivity of C_{2+} alcohols.[5–8] Among the various C_{2+} alcohol products,[6,7] ethanol (EtOH) has received widespread attention in recent years as an alternative fuel,[9–11] promising hydrogen carrier,[9,12] and versatile building block chemical for producing high-value products.[9,13–15] EtOH generation not only involves competition from several parallel reactions, including the formation of C_{2+} hydrocarbons and methanol, but also requires precise control of the dissociative and non-dissociative activation of C–O bonds to obtain surface alkyl and CO (H) species, respectively.[5,6,12,16] Therefore, achieving high selectivity and yield toward EtOH is challenging but urgently desired for future CO_2 utilization.[5,9,13,14]

Various catalytic systems have been reported for the hydrogenation of CO_2 into EtOH. Among these catalytic materials, noble-metal-based catalysts (Pd[17–20] and Rh[21–25]) are usually applied to promote C–O activation and the subsequent C–C coupling for EtOH synthesis.[7,13] The high price of noble metal catalysts limits their further application; thus, researchers have shifted their attention to 3d transition metal catalysts, such as Cu-,[19,26–29] Fe-,[30–34] and Co[4,35–38]-based catalysts, coupled with promoter elements such as alkali metal oxides. Among the 3d transition metal catalysts, Fe–Cu catalysts stand out as a cost-effective option with exceptional catalytic activity to produce C_{2+} alcohols from CO_2.[30,32,39] However, they also generate a substantial amount of hydrocarbons as byproducts.[32,39,40] Although some recent work has suggested that the introduction of Zn into Cs-promoted Fe–Cu based catalysts would be more efficient in producing EtOH,[30] the catalytic performance does not meet industrial requirements. In addition, little is known about the role of each element. Further improvements in the catalyst systems are essential for developing industrially valuable reaction processes.

Herein, we present a highly efficient catalytic system, namely K-promoted FeCuZn/ZrO_2 (KFeCuZn/ZrO_2), which significantly enhances the rate of EtOH production through CO_2 hydrogenation. Under optimized conditions (360 °C, 4 MPa, and 12 L g_{cat}^{-1} h^{-1}), our catalyst (KFeCuZn/ZrO_2) exhibits high activity (STY_{EtOH}: 5.4 mmol g_{cat}^{-1} h^{-1}) in the EtOH synthesis, compared to different supports. We thoroughly investigated the role of each constituent element using *in situ*/*operando* spectroscopic techniques and various characterizations.

[a]*Institute for Catalysis, Hokkaido University, Sapporo 001-0021, Japan. E-mail: toyao@cat.hokudai.ac.jp; Abdellah@cat.hokudai.ac.jp; kshimizu@cat.hokudai.ac.jp*

[b]*National Institute of Advanced Industrial Science and Technology (AIST), Research Institute for Chemical Process Technology, 4-2-1 Nigatake, Miyagino, Sendai 983-8551, Japan*

† Electronic supplementary information (ESI) available. See DOI: https://doi.org/10.1039/d4sc02588a

Experimental details

Chemicals and catalyst preparation

Chemicals and materials were purchased from commercial suppliers and used without further purification. ZrO_2 (RC-100), equivalent to JRC-ZRO-3, was supplied by Daiichi Kigenso Kagaku Kogyo. TiO_2 (P25) was obtained from Evonik. γ-Al_2O_3 (Puralox) was obtained from Sasol. SiO_2 (CariACT Q-10) was purchased from Fuji Silysia Chemical Company, Ltd.

KFeCuZn/support catalysts were prepared using a simple impregnation method. In this process, the support material was impregnated with an aqueous solution of KNO_3 (>98%; Wako Pure Chemical Industries), Fe $(NO_3)_3 \cdot 9H_2O$ (>98%; Wako Pure Chemical Industries), Zn $(NO_3)_2 \cdot 6H_2O$ (>98%; Kanto Chemical), and Cu $(NO_3)_2 \cdot 3H_2O$ (>99%; Aldrich). For example, KFeCuZn/ZrO_2 (3, 15, 10, and 5% wt of K, Fe, Zn, and Cu, respectively) was prepared by adding a certain amount of K, Fe, Cu, and Zn precursors and ZrO_2 to a glass vessel (100 mL) containing 20 mL of deionized water. The mixture was stirred at 200 rpm for 60 min at room temperature. Subsequently, water was removed from the mixture by evaporation *in vacuo*, followed by drying at 120 °C under ambient pressure, for ~12 h. The resulting material was calcined for 3 h at 500 °C in air.

Characterization

X-ray diffraction (XRD) analysis was conducted on a Miniflex (Rigaku) diffractometer using Cu Kα radiation. High-angle annular dark-field scanning transmission electron microscopy (HAADF-STEM) and energy-dispersive X-ray spectroscopy (EDS) were performed using an FEI Titan G2 microscope. The samples were prepared by dropping an ethanolic solution containing a catalyst onto carbon-supported Mo grids. N_2 adsorption measurements were conducted using an AUTOSORB 6AG (Yuasa Ionics) instrument at 77 K. Before the measurements, the calcined pieces of samples were ground and outgassed under vacuum at 200 °C for 3 h. The specific surface areas and pore size distribution of our samples were acquired by the Brunauer–Emmett–Teller (BET) N_2 adsorption measurements.

H_2 temperature-programmed reduction (H_2-TPR) was performed on a BELCat II instrument with a TCD detector. Briefly, ~100 mg of the catalyst was placed into a quartz tube and purged with Ar at 200 °C (2 h) to remove physically adsorbed water and surface carbonates. Then, the sample was cooled to 50 °C, followed by subsequent heating to 800 °C in 10 vol% H_2 balanced with Ar, at a ramping rate of 10 °C min^{-1}.

CO_2 temperature programmed surface reaction (CO_2-TPSR) was conducted on a BELCat II instrument with a mass spectrometer (BELMass; MicrotracBEL Corp). ~100 mg of catalyst was placed in a quartz tube and reduced by 10% H_2/Ar at 400 °C for 0.5 hours. The carrier gas was then changed to He and the sample cooled to 50 °C. Subsequently, 10% CO_2/He was introduced to allow CO_2 adsorption on the catalyst surface for 1 hour. The sample was then heated to 700 °C in a mixture of 10% H_2/Ar at a ramp rate of 10 °C min^{-1}. Ion fragmentation was monitored by BELMass at $m/z = 40$ for Ar, $m/z = 15$ for CH_4, $m/z = 28$ for CO and $m/z = 44$ for CO_2.

Pulse hydrogenation measurements were performed in a fixed-bed reactor. In detail, 100 mg of the used KFeCuZn/ZrO_2 catalyst was reactivated under the reaction gas (40 mL min^{-1}) at 320 °C for 1 h. After that, a pulse of CH_3CHO (500 μL for every injection) was introduced every 10 min for four cycles under a carrier gas (H_2/CO_2/Ar in a ratio of 74.4/24.8/0.8 and the total flow rate is 40 mL min^{-1}). The signals of CH_3CHO and CH_3-CH_2OH were monitored using an online mass spectrometer.

In situ/*operando* diffuse reflectance infrared Fourier transform (DRIFT) spectra were recorded on a JASCO FT/IR-4600 instrument equipped with a mercury–cadmium–telluride (MCT) detector. The sample was pressed into a DRIFT cell (DR-650 Ci) using a CaF_2 window. The spectra were measured by accumulating 20 scans at a resolution of 8 cm^{-1}, 0.5 MPa and temperature range of 200–320 °C. The reference spectrum in He flow (20 scans), taken at the measurement temperature, was subtracted from each spectrum. A high-sampling-rate GC-TCD (490 Micro GC; Agilent Technologies Inc.) was installed at the outlet for the analysis of methanol and ethanol.

Fe K-edge, Cu K-edge, and Zn K-edge X-ray absorption spectroscopy (XAS) were performed in transmission mode at BL01B1 of SPring-8 at the Japan Synchrotron Radiation Research Institute (JASRI) (Proposal No.: 2023A1931). A Si (111) double crystal monochromator was used. Boron nitride (BN) was used to make a pellet sample when the required amount was less than 20 mg. The spectra of reference compounds were recorded at room temperature, in air. The obtained XAS spectra were analyzed using the Athena and Artemis software ver. 0.9.26, included in the Demeter package.[41]

For *in situ* XAS measurements, samples in pellet forms (φ: 7 mm) were introduced into a cell equipped with Kapton film windows and gas lines connected to the micro-gas chromatograph. Pretreatment of the samples involved heating under a flow of H_2 (300 mL min^{-1}) at 300 °C for 30 min. Subsequently, 25% CO_2/He (400 mL min^{-1}), 75% H_2/He (400 mL min^{-1}), and CO_2 (100 mL min^{-1}) + H_2 (300 mL min^{-1}) were introduced into the cell with He purge intervals between gas introductions.

Catalytic reaction

CO_2 hydrogenation reactions were conducted in a fixed-bed continuous-flow reactor operating at a total pressure of 4 MPa (40 bar). We used 1% Ar/99% H_2 (purity; H_2: 99.99999%, Ar: 99.9999%) and CO_2 (purity; 99.995%) gas cylinders to supply the reaction gases. The reactor was supplied with a gas mixture of H_2/CO_2/Ar in a ratio of 74.4/24.8/0.8, with Ar serving as an internal standard gas. Prior to the catalytic measurements, 200 mg of the catalyst was placed between quartz wool inside a 1/4 inch fixed-bed reactor (inside diameter: 3.79 mm). The catalyst was pretreated under ambient pressure at a H_2/Ar (99%) flow rate of 20 mL min^{-1} and temperature of 400 °C for 0.5 h. Following the pretreatment, a H_2/CO_2/Ar (74.4/24.8/0.8) flow at a total flow rate of 40 mL min^{-1} was passed through the catalyst bed at 4 MPa. The weight hourly space velocity (WHSV) was 12 L g_{cat}^{-1} h^{-1}. We conducted an aging treatment for 10 h at 400 °C under the reaction gas atmosphere as an accelerated aging test before recording the results of the catalytic reaction (Fig. S1†).

The products were analyzed using an online gas chromatograph (Shimadzu GC-2014) equipped with TCD (Shincarbon-ST column) and FID (Porapak Q column) detectors, within a reaction temperature range of 240–400 °C.

The CO_2 conversion (X_{CO_2}) was calculated as follows.

$$X_{CO_2} = \frac{\frac{c^{in}_{CO_2}}{c^{in}_{Ar}} - \frac{c^{out}_{CO_2}}{c^{out}_{Ar}}}{\frac{c^{in}_{CO_2}}{c^{in}_{Ar}}} \times 100\%$$

The selectivity (S_i) for individual products was calculated by the following equation:

$$S_i = \frac{c_i \times n_i}{\sum(c_i \times n_i)} \times 100\%$$

Here, c_i is the molar fraction of product i (CO, hydrocarbons, or oxygenates), and n_i is the carbon number of product i in the reaction.

The EtOH decomposition experiments were conducted in a batch reactor using the spent catalyst. The spent catalyst (50 mg) was placed in a quartz tube and reduced using H_2 at 300 °C for 30 min. Subsequently, ethanol (0.3 mL) and octane (0.7 mL) were introduced into the quartz tube and fixed in a batch reactor. The above mixture was magnetically stirred at 260 °C under N_2 (0.5 MPa) for 3 h. Gas-phase products were collected and analyzed using a GC-FID (Shimadzu GC-2014; Porapak Q column) with a methanizer (Shimadzu MTN-1), whereas the liquid-phase products were analyzed using a gas chromatograph with a GC-FID (Shimadzu GC-14B; Ultra ALLOY capillary column UA$^+$-1; Frontier Laboratories, Ltd).

CO hydrogenation and additional CO_2 hydrogenation over the KFeCuZn/ZrO_2 catalyst reactions were conducted in the same fixed-bed continuous-flow reactor with the same WHSV (18.45 L g_{cat}^{-1} h^{-1}) and operated at the same pressure of 3 MPa for comparison. The reactor was supplied with a gas mixture of H_2/CO (CO_2)/Ar in a ratio of 74.4/24.8/0.8 (CO or CO_2 : H_2 = 1 : 3), with Ar serving as an internal standard gas. We conducted an aging treatment for 10 h at 400 °C under the reaction gas atmosphere as an accelerated aging test before recording the results of the catalytic reaction (as described in Fig. S1†). The products were analyzed using an online gas chromatograph (Shimadzu GC-2014) equipped with TCD (Shincarbon-ST column) and FID (Porapak Q column) detectors, within a reaction temperature range of 240–400 °C.

Results and discussion

Catalytic CO_2 hydrogenation to EtOH

CO_2 hydrogenation reactions were conducted under specific operating conditions of P = 4 MPa, T = 280–400 °C, and WHSV = 12 L g_{cat}^{-1} h^{-1}. As shown in Fig. 1a, the KFeCuZn/ZrO_2 catalyst exhibits the highest selectivity towards C_{2+} alcohol products, with ~40 and 16.5% selectivity towards C_{2+} alcohols and EtOH, respectively, while achieving a CO_2 conversion of 52.4%. In particular, the KFeCuZn/ZrO_2 catalyst also displays an excellent space time yield (STY) of EtOH, with a STY_{EtOH} of 5.4 mmol g_{cat}^{-1} h^{-1}. In comparison, the CO_2 conversion fell within a comparable range of 49.6–56.7% for the other studied catalysts (KFe/ZrO_2, KFeCu/ZrO_2 and KFeZn/ZrO_2). Additionally, for the Cu-added catalyst (KFeCu/ZrO_2), the EtOH selectivity was approximately 14%, accompanied by a high ethanol space-time yield (STY_{EtOH}) reaching up to 4.0 mmol g_{cat}^{-1} h^{-1}, which surpasses those of catalysts without Cu (KFe/ZrO_2 and KFeZn/ZrO_2). This suggests that Cu plays a significant role in facilitating the activation and coupling of CO_2 molecules for ethanol production.[40] Although the addition of Zn (KFeZn/ZrO_2) did not directly result in an obvious enhancement in EtOH production, the catalyst incorporating both Cu and Zn (KFeCuZn/ZrO_2) demonstrated the highest selectivity and STY_{EtOH}. Literature data on EtOH synthesis from CO_2/H_2 (Table S1†) are compared with our best catalytic system. Our catalyst displayed the best STY_{EtOH} for EtOH synthesis even after the accelerated aging test at 400 °C for 10 h.

To emphasize the pivotal roles of potassium and iron, we intentionally omitted these elements from the compared catalysts, as illustrated in Fig. 1a. Notably, the FeCuZn/ZrO_2 catalyst, while maintaining a CO_2 conversion of 47% comparable to that of the KFeZnCu/ZrO_2 catalyst, exhibited a significant increase in CH_4 selectivity, reaching 37%. Simultaneously, the selectivity for total alcohols and EtOH decreased sharply to 9 and 3.4%, respectively. Furthermore, the STY_{EtOH} for the FeCuZn/ZrO_2 catalyst was measured at 0.6 mmol g_{cat}^{-1} h^{-1}. This significantly reduced alcohol activity in the absence of K underscores the essential role of K in C_{2+} alcohol synthesis and the inhibition of over-hydrogenation.[34,39,40] The EtOH production significantly decreased over the KCuZn/ZrO_2 catalyst under the same

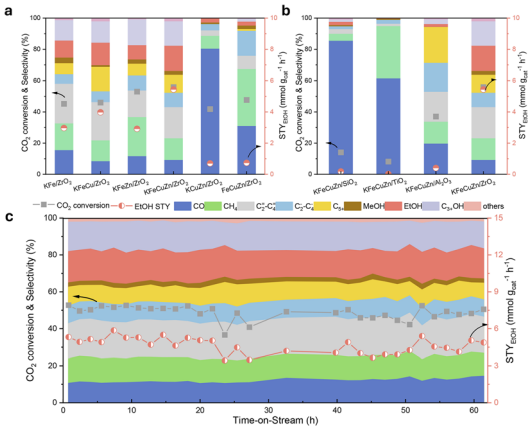

Fig. 1 Catalytic performance. (a) CO_2 conversion and product selectivity at 360 °C and STY_{EtOH} over KFe/ZrO_2 based catalysts; (b) CO_2 conversion, product selectivity, and STY_{EtOH} over different supporting; and (c) stability test for KFeCuZn/ZrO_2 at 360 °C. Pretreatment condition: 400 °C, 0.1 MPa, H_2 (99%), and 0.5 h. Reaction condition: 12 L g_{cat}^{-1} h^{-1}, 4.0 MPa, and H_2/CO_2/Ar (74.4/24.8/0.8%). Ar was used as an internal standard gas. The data was collected after 3 h, when the temperature and reaction were stable. Accelerated aging treatment was performed before reaction at 400 °C for 10 h under the reaction environment. Others include acetaldehyde and ethyl formate. In (a) and (b), the gray dot is CO_2 conversion; red dot is EtOH STY.

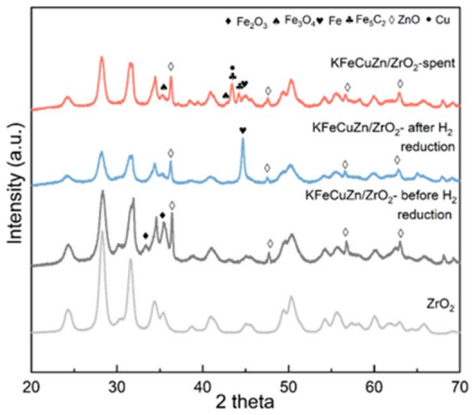

Fig. 2 XRD patterns of KFeCuZn/ZrO_2 before and after H_2 reduction at 400 °C as a pretreatment and after reaction. "Spent catalyst" refers to a sample that has undergone a 20 hours accelerated aging treatment at 400 °C under the reaction conditions.

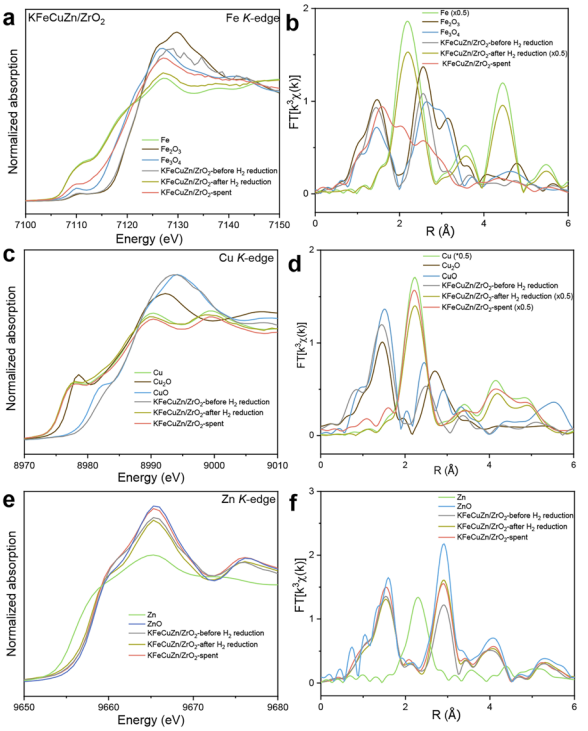

Fig. 3 *Ex situ* XAS spectra of KFeCuZn/ZrO_2 before and after H_2 reduction at 400 °C as a pretreatment and after reaction (spent). (a) Normalized Fe K-edge XANES spectra; (b) FT-EXAFS spectra for Fe; (c) normalized Cu K-edge XANES spectra; (d) FT-EXAFS spectra for Cu; (e) normalized Zn K-edge XANES spectra; and (f) FT-EXAFS spectra for Zn. "Spent catalyst" refers to a sample that has undergone a 20 hours accelerated aging treatment at 400 °C under the reaction condition.

conditions because of the absence of Fe, which resulted in the loss of the ability of the catalyst for C–C coupling.[42,43] Furthermore, Fig. S2† displayed a volcano-shaped curve for STY_{EtOH} with increasing Fe loading, and the most suitable loading is 15%$_{wt}$. Fig. 1b illustrates CO_2 hydrogenation experiments using different supports, such as Al_2O_3, TiO_2, and SiO_2. All three catalysts showed an obvious decrease in the EtOH selectivity to less than 2%. In terms of STY_{EtOH}, the KFeZnCu/ZrO_2 catalyst significantly outperformed the others, indicating that ZrO_2 is an excellent carrier for EtOH synthesis.

In addition, the effects of the reaction conditions, including reaction temperature, pressure, and WHSV, on EtOH synthesis were investigated in detail. On varying the reaction temperature within the range of 280–400 °C (Fig. S3†), the STY of EtOH and C_{2+} alcohol distribution exhibited a characteristic volcano-shaped curve. The appropriate temperature for acquiring EtOH is 360 °C. Additionally, the reaction pressure was varied from 3 to 5 MPa (Fig. S4a†), and the highest STY_{EtOH} (5.4 mmol g_{cat}^{-1} h^{-1}) were achieved at 4 MPa, making it a more favorable pressure regime for C_{2+} alcohol synthesis. Furthermore, we explored the influence of the WHSV (Fig. S4b†) by varying it between 9–15 L g_{cat}^{-1} h^{-1} and observed the most suitable WHSV was 12 L g_{cat}^{-1} h^{-1}. Moreover, the stability test was performed for the KFe-based catalysts (Fig. 1c and S5†). Among them, KFeCu/ZrO_2, KFeZn/ZrO_2 and KFeCuZn/ZrO_2 showed robust stability, maintaining their performance for at least 60 h at 360 °C. Only KFe/ZrO_2 displayed slight decrease in STY_{EtOH} after 35 h. Additionally, a simplified version of Fig. 1 was provided as Fig. S6,† by replacing the selectivity of $C_2^=$–$C_4^=$, C_2^-–C_4^-, and C_{5+} to C_{2+} hydrocarbons.

Structural characterization

Multiple characterization methods were used to reveal the physical characterizations and structural evolution. The BET specific surface areas and pore volumes (Table S2†), obtained from the N_2 adsorption measurements at 77 K, decreased upon increase in loading amount of the supported species. Pore size distributions were not significantly different among samples measured (Fig. S7†). XRD patterns (Fig. 2) show that the ZrO_2 support is composed of monoclinic and minor tetragonal phases based on the diffraction angles and intensities. Phase transformations of the loading elements were also observed at different reaction stages. For example, for the KFeCuZn/ZrO_2 catalyst, metallic Fe was obtained after H_2 reduction pretreatment (Fig. 2); subsequently, metallic Fe was oxidized to Fe_3O_4 and carburized to Fe_5C_2 after the reaction.[42,44] Iron carbide (Fe_5C_2) is an essential phase for C–C coupling in the Fischer–Tropsch (F–T) process over Fe-based catalysts.[42] Cu-derived peaks were not observed by XRD after calcination and reduction, probably due to the highly dispersed nature of Cu. Metallic copper was observed after the reaction owing to the sintering of Cu under a reductive atmosphere for a longer time. For the Zn species, only ZnO diffraction peaks were observed, indicating that no phase changes occurred during the entire reaction process. In comparison with the other control catalysts (Fig. S8†), the same evolution processes (reduction and carburization of Fe, reduction and aggregation of Cu, and stability of ZnO on Zn) were observed for the catalysts containing the relative elements.

To further clarify the phase transformations of Fe, Cu, and Zn species, X-ray adsorption spectroscopy (XAS) was performed

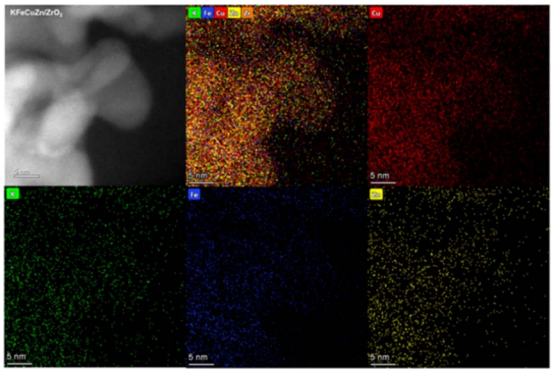

Fig. 4 HAADF-STEM image and corresponding EDS mapping images of the fresh $KFeCuZn/ZrO_2$ that has undergone calcination at 500 °C under air.

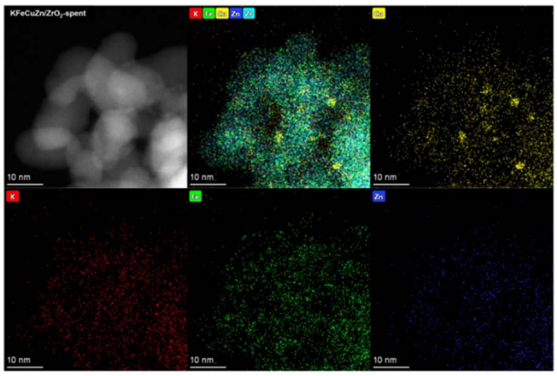

Fig. 5 HAADF-STEM image and corresponding EDS mapping images of the spent $KFeCuZn/ZrO_2$ that has undergone a 20 hours accelerated aging treatment at 400 °C under the reaction condition.

on $KFeCuZn/ZrO_2$. The *ex situ* X-ray absorption near edge structure (XANES) spectra of the Fe K-edge (Fig. 3a) show that after H_2 reduction as the pretreatment, the absorption edge shifted to almost the same energy as that of the Fe foil, suggesting that the Fe species in $KFeZnCu/ZrO_2$ were completely reduced. Similarly, after the reaction, the absorption edge moved to a higher energy compared to that of the Fe foil, suggesting the partial oxidation of Fe, in line with the XRD results. Extended X-ray absorption fine structure (EXAFS) results further helped to understand the local environmental changes (Fig. 3b and Table S3†). After the H_2 reduction pretreatment, the Fe–Fe bonds at 2.45 and 2.83 Å appeared, whereas the Fe–O bond at 1.99 Å disappeared.[45,46] After the reaction, Fe–C and Fe–O appeared, and the Fe–Fe bond weakened, indicating the generation of FeO_x and FeC_x, consistent with the XRD results. In the case of Cu (Fig. 3c), as exhibited in *ex situ* XANES spectra, CuO was reduced to metallic Cu after reduction, which was maintained until the end of the reaction, as supported by the curve fitting of the EXAFS spectra (Fig. 3d and Table S4†). Additionally, as indicated by the Zn K-edge XANES (Fig. 3e), after reduction, a weak shift to a lower energy was observed, implying the presence of a minor amount of metallic Zn, as confirmed by the EXAFS curve fitting results (Fig. 3f and Table S5†). In contrast, after the reaction, the energy increased to that of the closed ZnO reference and only one component of ZnO was captured (Table S5†), indicating that the zinc species prefers oxygen over hydrogen.[47]

H_2-TPR experiments were carried out to clarify the reduction ability of different additive elements and H_2 activation capacity over different catalysts. As depicted in Fig. S9,† considering mono-component supported catalysts such as Fe/ZrO_2, Cu/ZrO_2, and Zn/ZrO_2, Cu displayed the lowest reduction temperature and was the most readily reduced element, followed by Fe. In agreement with the XRD and XAS results, no reduction was observed in the ZnO content. In contrast, the introduction of K could promoted the generation of reduction peak at 600 °C, unlike with pure ZrO_2.[40] Contrastingly, after loading the promoter, the reduction temperatures of Fe and Cu increased for KFe/ZrO_2 and KCu/ZrO_2, inhibiting the reduction of the active elements.[39,40] Furthermore, in comparison with KFe/ZrO_2 and $KFeCu/ZrO_2$, the temperature for the reduction of Fe_2O_3 to Fe_3O_4 on the $KFeCu/ZrO_2$ catalyst decreased to 390 °C.[48] In contrast, the reduction temperature of FeO_x remained virtually unchanged over the $KFeZn/ZrO_2$ catalyst, suggesting that the introduction of Zn was ineffective in promoting the reduction of the Fe species. However, after loading Zn into $KFeCu/ZrO_2$, the reduction temperature increased slightly, indicating that the introduction of Zn led to a decrease in the reduction ability.[47,49]

HAADF-STEM and EDS were performed for fresh and spent $KFeCuZn/ZrO_2$, as shown in Fig. 4 and 5, respectively. Because of the weak *Z*-contrast, identifying the crystal phase and interplanar spacing of the Fe, Cu, and Zn species was challenging. Therefore, we only observed the elemental distributions. The HAADF-STEM and EDS elemental mapping images revealed that K, Fe, Cu, and Zn over the $KFeCuZn/ZrO_2$ catalyst were homogeneously distributed on ZrO_2 for fresh $KFeCuZn/ZrO_2$

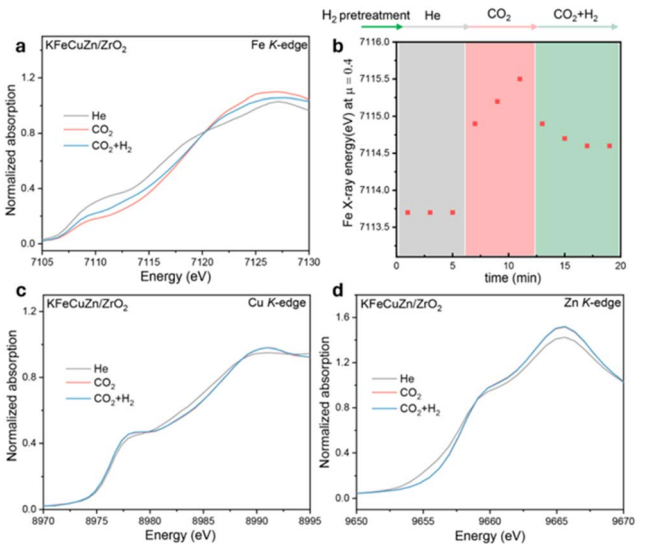

Fig. 6 *In situ* XAFS spectra of $KFeCuZn/ZrO_2$. (a) Normalized Fe K-edge XANES spectra; (b) X-ray energy at normalized absorption (μ = 0.4) under different atmospheres; (c) Cu K-edge XANES spectra; and (d) Zn K-edge XANES spectra. Conditions: 400 °C and 1 bar.

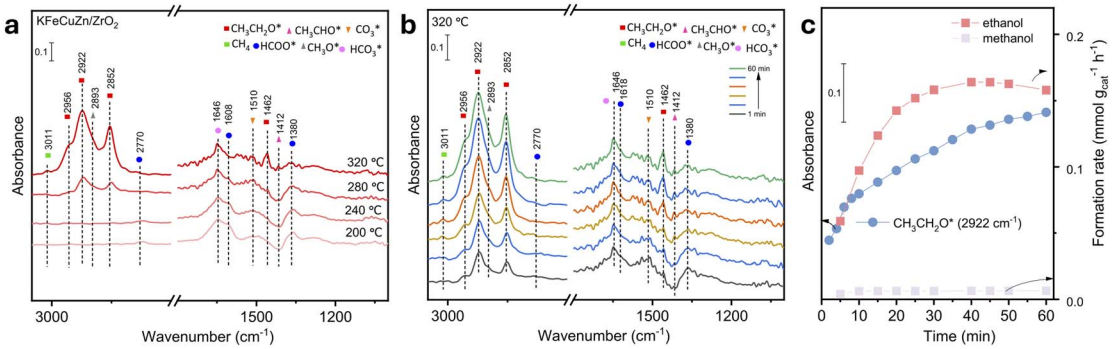

Fig. 7 *In situ*/*operando* DRIFTS spectra. (a) DRIFTS spectra of the CO_2 + H_2 reaction over KFeCuZn/ZrO_2 after 60 min at 0.5 MPa and different temperatures; (b) time resolution spectra of the CO_2 + H_2 reaction over KFeCuZn/ZrO_2 at 0.5 MPa and 320 °C; (c) dynamic IR peak intensities of CH_3CH_2O* (2922 cm^{-1}) and formation rate of ethanol and methanol, quantified by micro-GC at 320 °C.

(Fig. 4). After the reaction, K, Fe, and Zn remained highly dispersed in ZrO_2 (Fig. S10† and 5). The particle size of Cu increased a little, indicating the aggregation of Cu over KFeCuZn/ZrO_2. In comparison, larger Cu nanoparticles were observed over the spent KFeCu/ZrO_2, elucidating that the introduction of Zn limited Cu sintering (Fig. 5 and S11–S13†). Inhibition of sintering of Cu nanoparticles was also reported for Cs–CuZnFe[30] and CuZnO–Al_2O_3 (ref. 50) systems.

Mechanistic studies

In situ XAS was employed to clarify the chemical states under He, CO_2, and CO_2 + H_2 atmospheres at 400 °C and ambient pressure after H_2 pretreatment. The Fe K-edge XANES spectra (Fig. 6a) of KFeCuZn/ZrO_2 clearly showed that the absorption edge shifted to higher energies after the introduction of CO_2 (Fig. 6b), indicating that the Fe species were oxidized by CO_2. These results clearly proved that CO_2 functioned as an oxidizing agent, facilitating the oxidation of Fe species.[51]

For the Cu K-edge and Zn K-edge, although there were minor shifts upon the introduction of CO_2, the edge positions remained almost unchanged upon the introduction of CO_2 + H_2. These results suggested that the redox reactions of Cu and Zn were not involved in the CO_2 hydrogenation reaction.

The *in situ*/*operando* DRIFTS was performed to elucidate the mechanism underlying the hydrogenation of CO_2 to EtOH and role of each element. These *in situ*/*operando* DRIFTS experiments were conducted under specific conditions, including a pressure of 0.5 MPa, temperature of 320 °C (with an exception for KFeCuZn/ZrO_2, where the temperature range was 200–320 °C), and H_2 : CO_2 ratio of 3 : 1. The critical assignments of the surface species and adsorbed methanol and ethanol species are provided in Table S6 and Fig. S14.† Observations at 200 °C for KFeCuZn/ZrO_2 indicate the presence of adsorbed CO_2 at 1269 and 1514 cm^{-1},[30,52] which can be attributed to the carbonate species (bicarbonate species at 1620 cm^{-1})[53] and surface formate located at 2775/1593/1393 cm^{-1}.[22,40,54] No CH_3O* or CH_3CH_2O* were detected (Fig. S15a† and 7a). After the reaction temperature increased to 240 °C (Fig. S15b†), a weak peak, which can be attributed to an important intermediate of CH_3CHO* in EtOH synthesis, was observed at 1410 cm^{-1}.[40] When the temperature reached 280 °C (Fig. S16a†), with an increase in the exposure time, the intensity of the CH_3CHO* assignment gradually increased at 1410 cm^{-1}. After ~25 min, it was consumed, and subsequently, peaks assignable to ethoxy (2852/2922/2956 cm^{-1}) were observed.[27,30,39] In addition, EtOH in gas phase was tracked and quantified using online gas chromatography (Fig. S16b†). A CH_3CHO pulse experiment was also performed in a CO_2 + H_2 environment using the spent KFeZnCu/ZrO_2 catalyst (Fig. S17†). The introduction of CH_3CHO into the reaction environment resulted in a rapid increase in the intensity of the CH_3CH_2OH signal. This clearly indicates that the hydrogenation of CH_3CHO to CH_3CH_2OH is highly facile under the given conditions. Furthermore, the DRIFTS spectra also showed a minor peak at 2820 cm^{-1}, which can be assigned to CH_3O*,[30,54] along with a decrease in the intensity of the peak at 2770 cm^{-1}, assignable to formate. Upon reaching a temperature of 320 °C, the intensity of CH_3CH_2O* became more pronounced (Fig. 7b). In addition, another assignment appeared, with CH_3CH_2O* characterized by $\delta(CH_2)$ vibrations at 1462 cm^{-1}.[40] The methane appeared at 3011 cm^{-1},[39,40] which was not seen at lower temperatures. Notably, some papers reported that the peaks for CH_3CH_2O* and CH_3O* overlapped in the 2940–2980 cm^{-1} region.[27,30] According to the quantification of the micro-GC results the formation rate of EtOH was much higher than that of methanol (Fig. 7c). Thus, we assigned the peaks at 2852, 2922, and

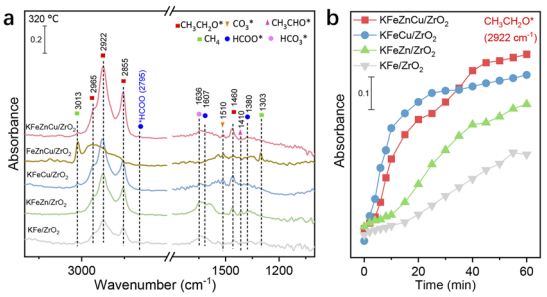

Fig. 8 *In situ* DRIFTS spectra. (a) Different catalysts under the CO_2 + H_2 reaction after 60 min at 320 °C and 0.5 MPa; (b) dynamic IR peak intensities of CH_3CH_2O* (2922 cm^{-1}) at 320 °C for different catalysts.

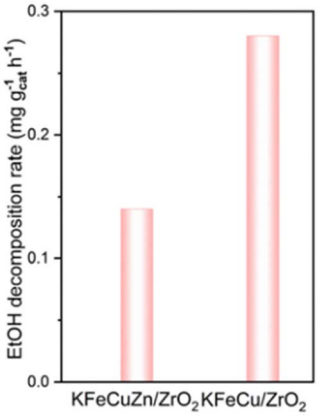

Fig. 9 EtOH decomposition over the KFeCuZn/ZrO_2 and KFeCu/ZrO_2 catalysts (conditions: batch reactor, spent catalysts: 50 mg, N_2: 0.5 MPa, at 260 °C, 3 h, ethanol (0.3 mL) + octane (0.7 mL)).

2956 cm^{-1} to CH_3CH_2O*, which is regarded as an important intermediate for EtOH formation.[27,30]

DRIFTS experiments were also conducted on various catalysts to identify the roles of the different elements. KFeCuZn/ZrO_2 catalyst displayed the highest CH_3CH_2O* intensity after 60 min (Fig. 8a). In comparison, the FeCuZn/ZrO_2 catalyst exhibited strong CH_4 peaks at 1302 and 3011 cm^{-1} during DRIFTS analysis (Fig. 8a and S18†),[55] which indicated K enabled suppression of CH_4 formation.[40,56] Simultaneously, there was a significant decrease in produced EtOH, the amount of adsorbed carbonate[30,52] at 1268 and 1510 cm^{-1} and formate species[22,40,54] at 1388 and 1594 cm^{-1}. These results indicate that the addition of potassium has a positive impact on enhancing CO_2 adsorption/activation and facilitates alcohol synthesis. In contrast, KFe/ZrO_2, KFeZn/ZrO_2, and KFeCu/ZrO_2 showed similar surface species but with variations in intensity compared to the KFeCuZn/ZrO_2 catalyst, indicating the same mechanism with different efficiencies (Fig. 8a and S19†). The evolution of CH_3CH_2O* is shown in Fig. 8b. The peak intensities of CH_3CH_2O* over KFeCuZn/ZrO_2 and KFeCu/ZrO_2 are similar and higher than those of the catalysts without Cu. This indicates that the addition of Cu is helpful for the evolution of CH_3CH_2O*, leading to EtOH formation. Concretely, introduction of Cu significantly promotes the formation of CO (CO_2-TPSR, Fig. S20†). It was reported[30,39,40,46] that increased CO provides a great chance of coupling with CH_x on iron carbide surface to form CH_3CHO, which in turn is hydrogenated to CH_3CH_2O* and subsequently CH_3CH_2OH, over Fe–Cu based catalysts. Because of the similar catalyst components, it is thought that EtOH was produced *via* the same pathway over our catalyst. Simultaneously, as previously reported, Cu helps non-dissociative activation of CO and its coupling with alkyl (CH_x) species to form ethanol.[30,39,40,46] Therefore, for KFe/ZrO_2 and KFeZn/ZrO_2 catalysts, the lack of Cu would result in the slight increase of CO and CH_4 selectivity. Although the Zn-assisted KFeCu/ZrO_2 catalyst showed a higher selectivity for EtOH and STY_{EtOH}, the difference between KFeCuZn/ZrO_2 and KFeCu/ZrO_2 remains unclear, according to DRIFT results (Fig. 1a).

CO_2 adsorption and EtOH decomposition experiments were conducted to elucidate the role and impact of Zn in EtOH synthesis. The DRIFTS results for CO_2 adsorption (Fig. S21†) revealed that the addition of Zn to the KFeZn/ZrO_2 and KFeCuZn/ZrO_2 catalysts enhanced CO_2 adsorption, leading to more formate and carbonates. The results of the ethanol decomposition experiments over KFeCu/ZrO_2 and KFeCuZn/ZrO_2 using a batch reactor are shown in Fig. 9. The carbonaceous products by the ethanol decomposition are CO_x, CH_4 and acetaldehyde over KFeCuZn/ZrO_2 and KFeCu/ZrO_2 catalysts, with the CH_3CH_2OH decomposition rate of 0.13 and 0.28 mg g_{cat}^{-1} h^{-1}, respectively. This result indicates that the presence of Zn restricts EtOH decomposition (backward reaction), leading to higher selectivity toward EtOH.

CO hydrogenation over KFeCuZn/ZrO_2

Although the one-step conversion of CO_2 to value-added chemicals such as EtOH is attractive, the kinetically unreactive and thermodynamically stable nature of CO_2 pose significant challenges.[8,28,57,58] CO hydrogenation to EtOH is another promising method for producing EtOH;[59–63] thus, we briefly explored the application of our catalysts in CO hydrogenation.[64–69] CO_2 and CO hydrogenation experiments were conducted on the KFeCuZn/ZrO_2 catalyst under the same

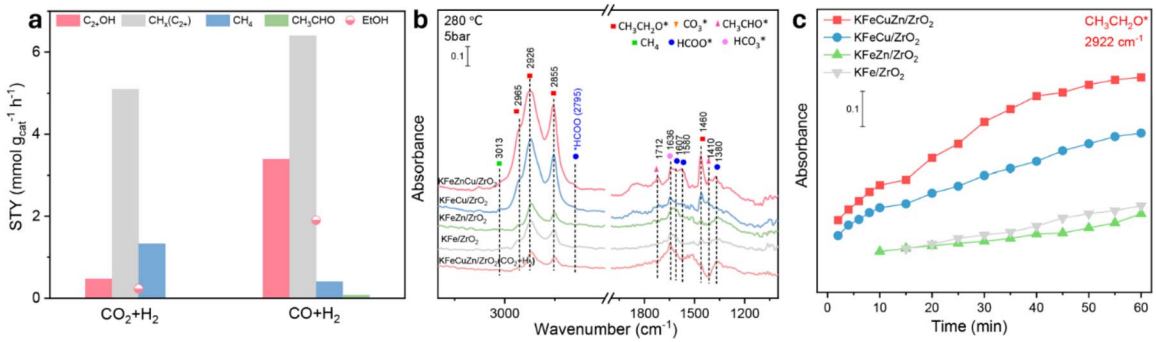

Fig. 10 (a) Catalytic performance over the KFeCuZn/ZrO_2 catalyst under a CO/H_2 or CO_2/H_2 flow at 280 °C and 3 MPa; (b) *in situ* DRIFTS spectra of the CO + H_2 reaction over the different catalysts under a CO/H_2 flow at 280 °C and 0.5 MPa; and (c) dynamic IR peak intensities of CH_3CH_2O* (2922 cm^{-1}) at 280 °C.

experimental conditions of 280 °C, 3 MPa, and CO or CO_2 : H_2 = 1 : 3. The performance results revealed a higher STY of EtOH (1.8 mmol g_{cat}^{-1} h^{-1}) in CO hydrogenation (Fig. 10a). Furthermore, in a comparison of the CO_2 + H_2 DRIFTS experiments, a higher amount of CH_3CH_2O* (2852, 2922, 2956 cm^{-1})[27,30] was observed in the CO_2 (20% CO) + H_2 DRIFTS experiments on KFeCuZn/ZrO_2 (Fig. S22†). These two experiments imply that CO hydrogenation to EtOH is more facile than CO_2 hydrogenation. In addition, CO + H_2 *in situ* DRIFTS was performed to clarify the potential roles of each element. According to the acquired IR spectra (Fig. 10b), the intermediates were similar to those observed in the CO_2 + H_2 DRIFTS results. The intensity of the peak at 1712 cm^{-1}, attributed to CH_3CHO* over KFeCuZn/ZrO_2, was found to be higher compared to the other catalysts.[30,70] Additionally, KFeCuZn/ZrO_2 displayed stronger peaks at 2852, 2922, and 2956 cm^{-1}, corresponding to CH_3CH_2O* (Fig. 10b, c and S23†), in comparison to the other catalysts.[27,30,39,40] The CH_3CH_2O* intensities of KFe/ZrO_2 and KFeZn/ZrO_2 were similar and much weaker than those of KFeCuZn/ZrO_2 (Fig. 10c).

Conclusion

In summary, we reported an efficient catalyst for ethanol synthesis, namely KFeCuZn/ZrO_2, which achieves the STY_{EtOH} of 5.4 mmol g_{cat}^{-1} h^{-1} under the optimized conditions (360 °C, 4 MPa, and 12 L g_{cat}^{-1} h^{-1}) and elucidated the essential roles of K, Fe, Cu, and Zn in EtOH synthesis. *In situ*/*operando* spectroscopic techniques and various characterizations revealed the essential roles of K and Fe in EtOH synthesis. The introduction of Cu accelerated the generation of CH_3CH_2O*, which is an important intermediate in EtOH production. The addition of Zn inhibited EtOH decomposition, thereby improving the efficiency of EtOH synthesis. The importance of all the components was proven and emphasized in CO_2 hydrogenation to EtOH. Finally, this catalyst demonstrated high performance in EtOH synthesis from syngas (CO + H_2).

Data availability

The data supporting this article have been included as part of the ESI.†

Author contributions

Takashi Toyao and Ken-ichi Shimizu supervised this research. Pengfei Du and Abdellah Ait El Fakir co-conducted the experiments and co-wrote the manuscript. Shirun Zhao, Yucheng Qian and HongLi Pan helped to perform the experiments and analyze the data. Nazmul Hasan MD Dostagir, Kah Wei Ting, and Shinya Mine discussed the data and commented on the manuscript.

Conflicts of interest

There are no conflicts of interest to declare.

Acknowledgements

This study was financially supported by KAKENHI (21K18185, 21H04626, 22K14538, 23KF0129, and 23H01997) from the Japan Society for the Promotion of Science (JSPS), JST-FOREST Program JPMJFR211U, the JST-SPRING project JPMJSP2119, "Nanotechnology Platform Program" of the Ministry of Education, Culture, Sports, Science and Technology (MEXT) project (JPMXP09A21HK0027), and the Joint Usage/Research Center for Catalysis. A. F. acknowledges a JSPS Postdoctoral Fellowship (P23351). The XAS measurements were conducted at the BL01B1 beamline of SPring-8 at JASRI (Proposal No.: 2023A1931).

References

1 S. S. Ali, S. S. Ali and N. Tabassum, *J. Environ. Chem. Eng.*, 2022, **10**, 106962.
2 P. Gao, S. Li, X. Bu, S. Dang, Z. Liu, H. Wang, L. Zhong, M. Qiu, C. Yang, J. Cai, W. Wei and Y. Sun, *Nat. Chem.*, 2017, **9**, 1019–1024.
3 T. Tatsumi, A. Muramatsu and H.-O. Tominaga, *Chem. Lett.*, 1985, 593–594.
4 M. Irshad, H. J. Chun, M. K. Khan, H. Jo, S. K. Kim and J. Kim, *Appl. Catal., B*, 2024, **340**, 123201.
5 D. Xu, Y. Wang, M. Ding, X. Hong, G. Liu and S. C. E. Tsang, *Chem*, 2021, **7**, 849–881.
6 A. I. Latsiou, N. D. Charisiou, Z. Frontistis, A. Bansode and M. A. Goula, *Catal. Today*, 2023, **420**, 114179.
7 S. Hafeez, E. Harkou, S. M. Al-Salem, M. A. Goula, N. Dimitratos, N. D. Charisiou, A. Villa, A. Bansode, G. Leeke, G. Manos and A. Constantinou, *React. Chem. Eng.*, 2022, **7**, 795–812.
8 Y. Wang, D. Xu, X. Zhang, X. Hong and G. Liu, *Catal. Sci. Technol.*, 2022, **12**, 1539–1550.
9 P. Iodice and M. Cardone, *Energies*, 2021, **14**, 4034.
10 M. A. S. Al-Baghdadi, *Renewable Energy*, 2003, **28**, 1471–1478.
11 D. Xu, H. Yang, X. Hong, G. Liu and S. C. Edman Tsang, *ACS Catal.*, 2021, **11**, 8978–8984.
12 S. Zhang, Z. Wu, X. Liu, K. Hua, Z. Shao, B. Wei, C. Huang, H. Wang and Y. Sun, *Top. Catal.*, 2021, **64**, 371–394.
13 X. Li, J. Ke, R. Li, P. Li, Q. Ma and T. S. Zhao, *Chem. Eng. Sci.*, 2023, **282**, 119226.
14 A. Z. Mendiburu, C. H. Lauermann, T. C. Hayashi, D. J. Mariños, R. B. Rodrigues da Costa, C. J. R. Coronado, J. J. Roberts and J. A. de Carvalho, *Energy*, 2022, **257**, 124688.
15 M. Al-Faliti, B. Dvorak and A. Aly Hassan, *J. Air Waste Manage. Assoc.*, 2022, **72**, 602–616.
16 T. Inui, T. Yamamoto, M. Inoue, H. Hara, T. Takeguchi and J.-B. Kim, *Appl. Catal., A*, 1999, **186**, 395–406.
17 Y. Lou, F. jiang, W. Zhu, L. Wang, T. Yao, S. Wang, B. Yang, B. Yang, Y. Zhu and X. Liu, *Appl. Catal., B*, 2021, **291**, 120122.
18 F. J. Caparrós, L. Soler, M. D. Rossell, I. Angurell, L. Piccolo, O. Rossell and J. Llorca, *ChemCatChem*, 2018, **10**, 2365–2369.
19 S. Bai, Q. Shao, P. Wang, Q. Dai, X. Wang and X. Huang, *J. Am. Chem. Soc.*, 2017, **139**, 6827–6830.

20 Y. Wang, Y. Zhou, X. Zhang, M. Wang, T. Liu, J. Wei, G. Zhang, X. Hong and G. Liu, *Appl. Catal., B*, 2024, **345**, 123691.
21 F. Zhang, W. Zhou, X. Xiong, Y. Wang, K. Cheng, J. Kang, Q. Zhang and Y. Wang, *J. Phys. Chem. C*, 2021, **125**, 24429–24439.
22 K. Zheng, Y. Li, B. Liu, F. Jiang, Y. Xu and X. Liu, *Angew. Chem., Int. Ed.*, 2022, **61**, e2022109.
23 A. Goryachev, A. Pustovarenko, G. Shterk, N. S. Alhajri, A. Jamal, M. Albuali, L. van Koppen, I. S. Khan, A. Russkikh, A. Ramirez, T. Shoinkhorova, E. J. M. Hensen and J. Gascon, *ChemCatChem*, 2021, **13**, 3324–3332.
24 X. Ye, J. Ma, W. Yu, X. Pan, C. Yang, C. Wang, Q. Liu and Y. Huang, *J. Energy Chem.*, 2022, **67**, 184–192.
25 H. Kusama, K. Okabe, K. Sayama and H. Arakawa, *Energy*, 1997, **22**, 343–348.
26 S. Liu, C. Yang, S. Zha, D. Sharapa, F. Studt, Z. J. Zhao and J. Gong, *Angew. Chem., Int. Ed.*, 2022, **61**, e202109027.
27 L. Ding, T. Shi, J. Gu, Y. Cui, Z. Zhang, C. Yang, T. Chen, M. Lin, P. Wang, N. Xue, L. Peng, X. Guo, Y. Zhu, Z. Chen and W. Ding, *Chem*, 2020, **6**, 2673–2689.
28 S. Li, H. Guo, C. Luo, H. Zhang, L. Xiong, X. Chen and L. Ma, *Catal. Lett.*, 2013, **143**, 345–355.
29 A. H. M. da Silva, L. H. Vieira, C. S. Santanta, M. T. M. Koper, E. M. Assaf, J. M. Assaf and J. F. Gomes, *Appl. Catal., B*, 2023, **324**, 122221.
30 D. Xu, M. Ding, X. Hong, G. Liu and S. C. E. Tsang, *ACS Catal.*, 2020, **10**, 5250–5260.
31 Y. Wang, W. Wang, R. He, M. Li, J. Zhang, F. Cao, J. Liu, S. Lin, X. Gao, G. Yang, M. Wang, T. Xing, T. Liu, Q. Liu, H. Hu, N. Tsubaki and M. Wu, *Angew. Chem., Int. Ed.*, 2023, **62**, e20231178.
32 W. Guo, W. G. Gao, H. Wang and J. J. Tian, *Adv. Mater. Res.*, 2014, **827**, 20–24.
33 Z. Si, L. Wang, Y. Han, J. Yu, Q. Ge, C. Zeng and J. Sun, *ACS Sustain. Chem. Eng.*, 2022, **10**, 14972–14979.
34 X. Xi, F. Zeng, H. Zhang, X. Wu, J. Ren, T. Bisswanger, C. Stampfer, J. P. Hofmann, R. Palkovits and H. J. Heeres, *ACS Sustain. Chem. Eng.*, 2021, **9**, 6235–6249.
35 H. Zhang, H. Han, L. Xiao and W. Wu, *ChemCatChem*, 2021, **13**, 3333–3339.
36 K. An, S. Zhang, J. Wang, Q. Liu, Z. Zhang and Y. Liu, *J. Energy Chem.*, 2021, **56**, 486–495.
37 P. Riani, G. Garbarino, T. Cavattoni and G. Busca, *Catal. Today*, 2021, **365**, 122–131.
38 S. Zhang, Z. Wu, X. Liu, Z. Shao, L. Xia, L. Zhong, H. Wang and Y. Sun, *Appl. Catal., B*, 2021, **293**, 120207.
39 D. Xu, M. Ding, X. Hong and G. Liu, *ACS Catal.*, 2020, **10**, 14516–14526.
40 T. Liu, D. Xu, M. Song, X. Hong and G. Liu, *ACS Catal.*, 2023, **13**, 4667–4674.
41 B. Ravel and M. Newville, *J. Synchrotron Radiat.*, 2005, **12**, 537–541.
42 C. Wang, W. Fang, Z. Liu, L. Wang, Z. Liao, Y. Yang, H. Li, L. Liu, H. Zhou, X. Qin, S. Xu, X. Chu, Y. Wang, A. Zheng and F. S. Xiao, *Nat. Nanotechnol.*, 2022, **17**, 714–720.
43 N. Lohitharn, J. G. Goodwin and E. Lotero, *J. Catal.*, 2008, **255**, 104–113.
44 N. Boreriboon, X. Jiang, C. Song and P. Prasassarakich, *Top. Catal.*, 2018, **61**, 1551–1562.
45 K. Asakura, M. Nomura and H. Kuroda, *Bull. Chem. Soc. Jpn.*, 1985, **58**, 1543–1550.
46 Y. Wang, K. Wang, B. Zhang, X. Peng, X. Gao, G. Yang, H. Hu, M. Wu and N. Tsubaki, *ACS Catal.*, 2021, **11**, 11742–11753.
47 L. R. Merte, G. Peng, R. Bechstein, F. Rieboldt, C. A. Farberow, L. C. Grabow, W. Kudernatsch, S. Wendt, E. Lægsgaard, M. Mavrikakis and F. Besenbacher, *Science*, 2012, **336**, 889–893.
48 D. Peña, L. Jensen, A. Cognigni, R. Myrstad, T. Neumayer, W. van Beek, M. Rønning, D. Peña, L. Jensen, T. Neumayer, A. Cognigni, M. Rønning and W. van Beek, *ChemCatChem*, 2018, **10**, 1300–1312.
49 F. Amet, C. T. Ke, I. V. Borzenets, J. Wang, K. Watanabe, T. Taniguchi, R. S. Deacon, M. Yamamoto, Y. Bomze, S. Tarucha and G. Finkelstein, *Science*, 2016, **352**, 966–969.
50 Š. Hajduk, V. D. B. C. Dasireddy, B. Likozar, G. Dražić and Z. C. Orel, *Appl. Catal., B*, 2017, **211**, 57–67.
51 P. Du, R. Qi, Y. Zhang, Q. Gu, X. Xu, Y. Tan, X. Liu, A. Wang, B. Zhu, B. Yang and T. Zhang, *Chem*, 2022, **8**, 3252–3262.
52 M. Mohtar and R. Omar, *Solid State Sci. Technol.*, 2005, **13**, 24–31.
53 N. H. M. Dostagir, R. Rattanawan, M. Gao, J. Ota, J. Y. Hasegawa, K. Asakura, A. Fukouka and A. Shrotri, *ACS Catal.*, 2021, **11**, 9450–9461.
54 X. Chang, X. Han, Y. Pan, Z. Hao, J. Chen, M. Li, J. Lv and X. Ma, *Ind. Eng. Chem. Res.*, 2022, **61**, 6872–6883.
55 J. Wu, S. Li, G. Li, C. Li Bv and Q. Xin, *Appl. Surf. Sci.*, 1994, **81**, 37–41.
56 M. Wang, P. Wang, G. Zhang, Z. Cheng, M. Zhang, Y. Liu, R. Li, J. Zhu, J. Wang, K. Bian, Y. Liu, F. Ding, T. P. Senftle, X. Nie, Q. Fu, C. Song and X. Guo, *Sci. Adv.*, 2023, **9**, eadg0167.
57 D. Goud, S. R. Churipard, D. Bagchi, A. K. Singh, M. Riyaz, C. P. Vinod and S. C. Peter, *ACS Catal.*, 2022, **12**, 11118–11128.
58 T. Inoue, T. Iizuka and K. Tanabe, *Appl. Catal.*, 1989, **46**, 1–9.
59 Y. Ge, T. Zou, A. J. Martín and J. Pérez-Ramírez, *ACS Catal.*, 2023, **13**, 9946–9959.
60 P. Preikschas, M. Plodinec, J. Bauer, R. Kraehnert, R. Naumann D'Alnoncourt, R. Schlögl, M. Driess and F. Rosowski, *ACS Catal.*, 2021, **11**, 4047–4060.
61 X. Wang, P. J. Ramírez, W. Liao, J. A. Rodriguez and P. Liu, *J. Am. Chem. Soc.*, 2021, **143**, 13103–13112.
62 J. Hu, Z. Wei, Y. Zhang, R. Huang, M. Zhang, K. Cheng, Q. Zhang, Y. Qi, Y. Li, J. Mao, J. Zhu, L. Wu, W. Wen, S. Yu, Y. Pan, J. Yang, X. Wei, L. Jiang, R. Si, L. Yu, Y. Wang and D. Deng, *Nat. Commun.*, 2023, **14**, 6808.
63 Y. Lu, F. Yu, J. Hu and J. Liu, *Appl. Catal., A*, 2012, **429–430**, 48–58.
64 M. Schumann, M. R. Nielsen, T. E. L. Smitshuysen, T. W. Hansen, C. D. Damsgaard, A. C. A. Yang, M. Cargnello, J. D. Grunwaldt, A. D. Jensen and J. M. Christensen, *ACS Catal.*, 2021, **11**, 5189–5201.

65 B. J. Kip, E. G. F. Hermans, J. H. M. C. Van Wolput, N. M. A. Hermans, J. Van Grondelle and R. Prins, *Appl. Catal.*, 1987, **35**, 109–139.
66 M. Gupta, M. L. Smith and J. J. Spivey, *ACS Catal.*, 2011, **1**, 641–656.
67 Y. Liu, K. Murata, M. Inaba, I. Takahara and K. Okabe, *Catal. Today*, 2011, **164**, 308–314.
68 T. Ishida, T. Yanagihara, X. Liu, H. Ohashi, A. Hamasaki, T. Honma, H. Oji, T. Yokoyama and M. Tokunaga, *Appl. Catal., A*, 2013, **458**, 145–154.
69 F. G. A. Van Den Berg, J. H. E. Glezer and W. M. H. Sachtler', *J. Catal.*, 1985, **93**, 340–352.
70 A. K. P. Mann, Z. Wu, F. C. Calaza and S. H. Overbury, *ACS Catal.*, 2014, **4**, 2437–2448.